coverage of more than 180° at teleseismic stations, and standard errors of less than 35 km in location and 15 km in depth. This procedure (E. R. Engdahl, R. D. van der Hilst, R. Buland, in preparation) ensures that depth errors and the mapping of source heterogeneity into mislocation are minimized, thereby creating a powerful uncontaminated database of *P*, *pP*, and *pwP* residuals for use in tomographic imaging.
18. R. D. van der Hilst, B. L. N. Kennett, D. Christie, J. Grant, *Trans. Am. Geophys. Union* **75**, 177 (1994).
19. For stations outside the study area, we combined all ray paths from earthquakes in a particular source region to closely spaced stations elsewhere into a single ray, commonly referred to as the summary ray, to reduce the uneven sampling of mantle structure by ray paths, the dimension of the matrices involved in the inversions (and thus computer memory requirements), and the computer time for ray tracing. The datum (residual time) assigned to the summary ray was the median of all data considered for that summary ray. The number of rays that contributed to the summary ray was not restricted. For stations inside the study area, however, we used individual rays to optimize the sampling.
20. W. Spakman, S. van der Lee, R. van der Hilst, *Phys. Earth Planet. Inter.* **79**, 3 (1993).
21. We inverted data from different time periods and from earthquakes in different depth intervals to test the robustness of structural information in the images. In addition, test inversions were conducted with synthetic data (with and without simulated data errors) computed from the ray distribution as in the real data inversion from isolated target anomalies, checkerboard patterns, and specifically designed, semirealistic slab models (*15*). One has to be cautious with the interpretation of the results of such tests because they do not simulate accurately the effect of data errors and source mislocation and because they are conducted with the same theoretical assumptions (for example, linearization and neglect of anisotropy) and approximations (for example, parameterization) as in the inversion of reported phase data. Interpretation is further complicated by the dependence of inferences pertinent to image quality on the spatial characteristics of the input model from which synthetic data were computed [J.-J. Léveque, L. Rivera, G. Wittlinger, *Geophys. J. Int.* **115**, 313 (1993)]. The neglect of the effects of the fast slab on wave velocity and ray path position can result in the overestimation of the thickness of the slab [E. R. Engdahl and D. Gubbins, *J. Geophys. Res.* **92**, 13855 (1987)] but probably does not produce an effect on the large-scale structures discussed here that is significant enough to invalidate our conclusions.
22. R. K. Cardwell and B. L. Isacks, *J. Geophys. Res.* **83**, 2825 (1978); P. Lundgren and D. Giardini, *ibid.* **99**, 15833 (1994).
23. The absence of earthquakes between 350 and 500 km in depth could be caused by the low deviatoric stress in the transition from tensional to compressional stress (*6, 8*) or to the weakening of the plate by the exothermic phase change from olivine to β spinel at ~410 km [D. C. Rubie, *Nature* **308**, 505 (1984); M. J. R. Wortel, *Geophys. Res. Lett.* **13**, 34 (1986)].
24. M. G. Audley-Charles, P. D. Ballantyne, R. Hall, *Tectonophysics* **155**, 317 (1988), and references therein.
25. E. J. Cobbing, D. I. J. Mallick, P. E. J. Pitfield, L. H. Teoh, *J. Geol. Soc. London* **143**, 537 (1986).
26. C. S. Hutchison, *Geol. Soc. Am. Bull.* **86**, 797 (1975).
27. M. Gurnis and B. H. Hager, *Nature* **335**, 317 (1988); C. Kincaid and P. Olson, *J. Geophys. Res.* **92**, 13832 (1987); R. W. Griffiths, R. Hackney, R. D. van der Hilst, *Earth Planet. Sci. Lett.* **133**, 1 (1995).
28. S. Zhong and M. Gurnis, *Science* **267**, 838 (1995); G. F. Davies, *Earth Planet. Sci. Lett.* **133**, 507 (1995); U. R. Christensen, in preparation.
29. U. R. Christensen and D. Yuen, *J. Geophys. Res.* **89**, 4389 (1984).
30. J. B. Minster and T. H. Jordan, *ibid.* **83**, 5331 (1978).
31. C. DeMets, R. G. Gordon, D. F. Argus, S. Stein, *Geophys. J. Int.* **101**, 425 (1990).
32. C.-S. Liu, J. R. Curray, J. M. McDonald, *Earth Planet. Sci. Lett.* **65**, 331 (1983); T. W. C. Hilde, S. Uyeda, L. Kroenke, *Tectonophyiscs* **38**, 145 (1977).
33. Oblique subduction below Sumatra is comparable to the oblique subduction of the Pacific Plate at the western Aleutian trench, for which K. C. Creager and T. M. Boyd [*J. Geophys. Res.* **96**, 2293 (1991)] showed from membrane strain calculations that the particle motion in the shallow slab is essentially subhorizontal.
34. M. J. R. Wortel and W. Spakman, *Proc. K. Ned. Akad. Wet.* **95**, 325 (1992).
35. After initiation of slab detachment, the gravitational force exerted on the detached slab results in an increased slab pull and tensional stress in the hinge area of the adjacent segment of continuous slab, which can lead to shear failure and the lateral propagation of the detachment [also see S. Yoshioka and M. J. R. Wortel, *J. Geophys. Res.* **100**, 20223 (1995); S. Yoshioka, D. A. Yuen, T. B. Larsen, *Island Arc* **4**, 89 (1995)]. As a result, the slab pull is small for the region of detachment, increases abruptly near the hinge region, and assumes normal values where the deep slab is still attached to the surface plate. The laterally migrating concentration of the tensional forces can also result in more pronounced slab roll back and oceanward trench migration, which has been invoked to explain block rotations in the Mediterranean region. In our case, the hinge region is near the transition from Sumatra to Java, close to 105°E.
36. We gratefully acknowledge J. Weekes for the excellent picking of phase arrivals in the *Skippy* records that were used in this study; B. L. N. Kennett, K. C. Creager, O. Gudmundsson, and anonymous referees for reviews; G. Nolet for providing us with his LSQR inversion code; and E. R. Engdahl for early versions of our hypocenter and phase data set. We thank C. Krayshek for producing the final draft of Fig. 4.

5 September 1995; accepted 29 December 1995

The Majorite-Pyrope + Magnesiowüstite Assemblage: Constraints on the History of Shock Veins in Chondrites

Ming Chen, Thomas G. Sharp, Ahmed El Goresy,* Brigitte Wopenka, Xiande Xie

Shock veins in the Sixiangkou (L6) chondrite contain two high-pressure assemblages: (i) majorite-pyrope solid solution plus magnesiowüstite that crystallized at high pressures and temperatures from a shock-induced silicate melt of bulk Sixiangkou composition and (ii) ringwoodite plus low-calcium majorite that were produced by solid-state transformation of olivine and low-calcium pyroxene. The morphology and chemistry of the majorite-pyrope garnet and the size of the magnesiowüstite crystals indicate a longer duration at high pressure and temperature than predicted by impact scenarios. This pressure-temperature regime is constrained by the olivine-ringwoodite and orthopyroxene-majorite phase transformations, fusion of the meteorite constituents, and crystallization of majorite-pyrope solid solution plus magnesiowüstite from that melt under high pressure.

Forsteritic olivine [Fe/(Fe+Mg) < 0.26] transforms into the denser polymorphs modified spinel (wadsleyite, β phase) and spinel (ringwoodite, γ phase) in the Earth's transition zone (*1–4*) and dissociates at pressures $P > 23$ GPa and temperatures $T \geq 1600$°C to perovskite plus magnesiowüstite in the Earth's lower mantle (*5*). Majorite ($Mg_4Si_4O_{12}$ garnet) is a stable phase in the pressure range 19 to 24 GPa at temperatures between 1700° and 2600°C and transforms to a perovskite-type structure at higher pressures (*6*). Along with experimental investigations at high pressures and temperatures, mineral assemblages in heavily shocked meteorites can reveal crucial information about phase transitions and high-pressure minerals (*7–9*). Unfortunately, our understanding of shock-induced phase transitions and the conditions of high pressure and temperature in shocked meteorites is limited by the fact that shock experiments do not produce such transformations. To understand the pressure and temperature conditions and the durations of shock events in chondrites, one must examine the minerals that crystallize from shock melts at high pressure as well as those formed by solid-state transformation. Shock melts in terrestrial and lunar rocks, for example, do not crystallize high-pressure minerals, whereas shock veins in chondrites do (*8, 10*). This difference suggests a distinction between the pressure-temperature histories of impact events on chondritic asteroids and those on the Earth and moon.

The heavily shocked Sixiangkou meteorite contains black veins, ranging in width from 0.1 to 2 mm, that consist of two lithologies: (i) mostly unfractured, rounded, large polycrystalline grains of ringwoodite and low-Ca majorite (15 to 300 μm in diameter), plus diaplectic plagioclase glass (10 to 60 μm in diameter), and (ii) a fine-grained matrix

M. Chen, Max-Planck-Institut für Kernphysik, Saupfercheckweg 1, D-69117 Heidelberg, Germany, and Guangzhou Institute of Geochemistry, Academia Sinica, 510640 Guangzhou, China.
T. G. Sharp, Bayerisches Geoinstitut, Universität Bayreuth, D-95440 Bayreuth, Germany.
A. El Goresy, Max-Planck-Institut für Kernphysik, Saupfercheckweg 1, D-69117 Heidelberg, Germany.
B. Wopenka, Department of Earth and Planetary Sciences, Washington University, St. Louis, MO 63130, USA.
X. Xie, Guangzhou Institute of Geochemistry, Academia Sinica, 510640 Guangzhou, China.

*To whom correspondence should be addressed.

(0.5- to 4-μm-diameter grains) of Al-, Na-, Ca-, and Cr-bearing majorite and dark isotropic material constituting more than 80% of the veins by volume (Fig. 1) (*8*). The fine-grained part of the vein is sprinkled with kamacite and troilite blebs or metal-troilite eutectic intergrowths. The isotropic material was initially interpreted to be silicate glass that was quenched with the majorite-pyrope solid solution from a silicate liquid (*8*). We used analytical transmission electron microscopy (TEM), scanning electron microscopy, and electron microprobe analyses (EMPA) to characterize the shock-vein minerals, which allowed us to constrain the history of the shock event on the L6 chondrite parent body.

The polycrystalline grains of ringwoodite [$(Mg_{1.49}Fe_{0.49}Mn_{0.01})SiO_4$] and the low-Ca majorite [$(Mg_{3.09}Fe_{0.82}Ca_{0.06}Mn_{0.03})Si_4O_{12}$] have the same compositions as olivine and low-Ca pyroxene, respectively, outside of the black shock veins (Table 1). Micro-Raman, TEM, and selected area electron diffraction (SAED) investigations showed that these grains are single-phase ringwoodite (γ-phase) and low-Ca majorite, respectively (*11*). Ringwoodite polycrystalline aggregates consist of grains ranging from 2 to 6 μm in size with abundant stacking faults and dislocations (Fig. 2). The stacking fault densities are similar to those seen in ringwoodites from other meteorites (*7*) and synthetic ringwoodites (*2*, *3*). Highly disordered spinelloid structures, such as those commonly found in partial-transformation experiments (*3*, *11*), were not observed. The average density of dislocations in ringwoodite is 8×10^{12} m^{-2}. The majorite aggregates contain grains up to 10 μm in size that are subdivided by well-organized walls of dislocations. This subgrain structure, similar to that seen in natural garnets from ultradeep-mantle xenoliths (*12*) and synthetic majorites (*13*), indicates plastic deformation by dislocation creep. Climb of dislocations into subgrain boundaries is a diffusion-controlled process that requires significant time at high temperatures (*14*). There is no evidence of twinning or tweed textures, which are common in tetragonal majorite (*13*, *15*, *16*), and all of the SAED patterns collected were consistent with cubic symmetry.

The fine-grained matrix consists of two lithologies: (i) a metal-troilite–poor lithology along the edges of the veins bordering the unshocked part of the meteorite (Fig. 1), and (ii) a metal-troilite–rich portion in the interior of the veins enclosing the large rounded grains of ringwoodite and low-Ca majorite. The predominant constituent of the metal-troilite–poor lithology is a majorite-pyrope solid solution that occurs as idiomorphic crystals ranging in size from 0.5 to 4 μm in diameter (Fig. 3). In contrast to the polycrystalline low-Ca majorite, these matrix garnets are rich in Al_2O_3, CaO, and Na_2O and contain appreciable amounts of Cr_2O_3, with majorite and pyrope as the major constituents (Table 1). Our TEM imaging and SAED

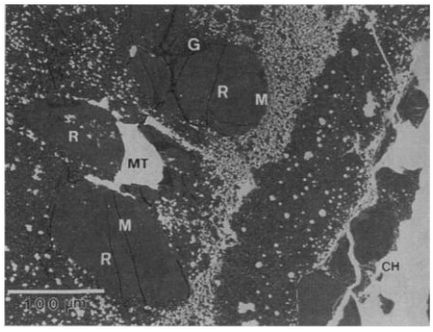

Fig. 1. Back-scattered electron image of a shock-induced vein in the Sixiangkou meteorite. The vein intersects normal chondritic material (CH) and consists of relatively large aggregate grains of ringwoodite (R) and low-Ca majorite (M), as well as diaplectic plagioclase glass (G) and metal-troilite eutectic intergrowths (MT) in a fine-grained matrix of silicate, oxide, and metal grains. The rounded outline of the silicate fragments is indicative of partial resorption into the molten matrix during the shock event.

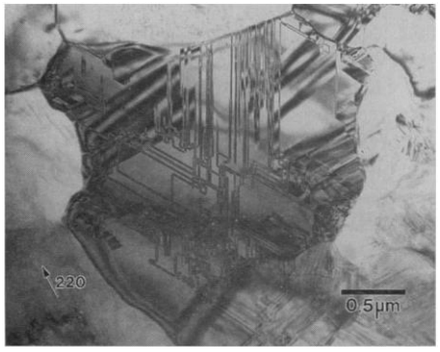

Fig. 2. Bright-field TEM image of a 3-μm ringwoodite grain obtained with the 220 reflection. Under these imaging conditions, the *a*/4 ⟨110⟩ {110} stacking faults (*a* is a crystal axis) on (101) and (01$\bar{1}$) are clearly visible.

Table 1. Average phase compositions for low-Ca pyroxene (px), low-Ca majorite (mj, $Mj_{97.5}Ca$-$Mj_{1.5}Py_{0.5}Uv_{0.5}$, where Uv is uvarovite), majorite-pyrope solid solution (mj-py, $Mj_{73.8}Na$-$Mj_{4.7}Ca$-$Mj_{4.2}Py_{15.8}Uv_{1.5}$), olivine (ol), ringwoodite (ri), magnesiowüstite (mw, $Wü_{54}$-Per_{46}, where Wü is wüstite and Per is periclase), and Sixiangkou bulk compositions. All values were determined by EMPA except mw, which was by TEM. All data are in weight %; the number in parentheses is the number of analyses (n.d., not detected). The formulas were calculated on the basis of fixed numbers of cations. Ranges for oxide concentrations that varied by more than 2%: mj: MgO 27.81 to 29.93; mj-py: FeO 9.16 to 13.42, SiO_2 50.26 to 53.01; ri: SiO_2 37.30 to 40.21, MgO 37.12 to 39.53. Standard deviations: SiO_2, 0.9; MgO, 0.67; CaO, 0.16; MnO, 0.02; FeO, 1.62; TiO_2, 0.67; Al_2O_3, 0.17; Cr_2O_3, 0.04; and Na_2O, 0.11. Bulk 1 is the bulk composition of the chondrite from (*27*) after subtraction of metal and troilite and recalculation to 100% (*28*). Bulk 2 is the average bulk composition of areas free of metal and troilite in the assemblage majorite-pyrope solid solution + magnesiowüstite, determined by a broad-beam (EMPA) technique.

Oxide	px (5)	mj (10)	mj-py (10)	ol (7)	ri (20)	mw (4)	Bulk 1 (1)	Bulk 2 (10)
SiO_2	54.83	54.74	52.18	38.02	38.18	1.11	45.21	47.53
MgO	27.65	28.65	28.02	38.19	38.23	34.85	28.49	26.39
CaO	0.95	0.78	2.19	0.04	0.03	n.d.	2.18	2.18
MnO	0.46	0.49	0.34	0.49	0.49	n.d.	0.41	0.40
FeO	14.16	13.61	11.45	22.25	22.42	62.85	18.39	17.17
TiO_2	0.17	0.20	0.11	0.01	0.02	0.29	0.12	0.18
Al_2O_3	0.15	0.17	3.67	0.01	0.01	n.d.	3.04	2.71
Cr_2O_3	0.13	0.13	0.55	0.04	0.03	0.86	0.64	0.53
Na_2O	0.04	0.04	0.99	n.d.	n.d.	n.d.	1.17	1.03
V_2O_3	0.02	n.d.	0.03	0.02	0.02	n.d.	0.13	0.03
K_2O	n.d.	n.d.	n.d.	n.d.	n.d.	n.d.	n.d.	n.d.
P_2O_5	n.d.	n.d.	n.d.	n.d.	n.d.	n.d.	0.23	n.d.
Totals	98.56	98.81	99.53	99.07	99.45	99.96	100.00	99.14
			Number of cations per formula unit					
Si	2.00	3.96	3.70	1.00	1.00	0.01	–	–
Mg	1.50	3.09	2.96	1.50	1.49	0.48	–	–
Ca	0.04	0.06	0.17	0.00	0.00	-	–	–
Mn	0.01	0.03	0.02	0.01	0.01	-	–	–
Fe	0.43	0.77	0.28	0.48	0.48	0.49	–	–
Ti	0.00	0.01	0.01	–	0.00	0.002	–	–
Al	0.01	0.01	0.31	–	–	–	–	–
Cr	0.00	0.01	0.03	0.00	0.00	0.006	–	–
Na	0.00	0.00	0.14	–	–	–	–	–
V	0.00	–	0.00	0.00	0.00	–	–	–
Fe^{3+}	0.01	0.05	0.39	0.01	0.01	–	–	–
Totals	4.00	7.99	8.01	3.00	2.99	0.988	–	–
Oxygens	6.01	11.99	11.81	4.00	4.00	1.0	–	–

of the majorite-pyrope solid solution showed no evidence of twinning or tetragonal symmetry. In the interstitial channels between these idiomorphic garnets, irregularly shaped blebs of magnesiowüstite [$(Mg_{0.54}Fe_{0.46})O$] up to 5 μm long were observed (Fig. 3), constituting 15 to 20% (by volume) of the metal-troilite–poor lithology. Our SAED analysis showed that these irregular magnesiowüstite blebs are segments of large, multibranched single crystals that fill the channels between several majorite-pyrope garnets. The relatively large size of the garnet and magnesiowüstite grains in the matrix suggests relatively low nucleation rates, which are not consistent with rapid quenching. Magnesiowüstite was observed in the Tenham chondrite (9) as inclusions in majorite-rich garnets, which were also interpreted as having crystallized from a shock melt at high pressure. Diffraction patterns from magnesiowüstite in Sixiangkou contain strong reflections corresponding to its NaCl structure and weak superstructure-like reflections halfway between the normal reflections. These extra reflections result from submicroscopic magnetite crystallites (as small as 3 nm) that are coherently intergrown throughout the magnesiowüstite and apparently exsolved out of nonstoichiometric magnesiowüstite during cooling.

The metal-rich and metal-poor matrix assemblages are relatively homogeneous

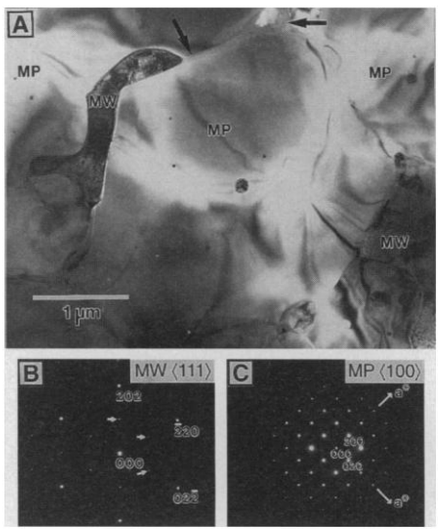

Fig. 3. (**A**) Bright-field TEM image of the shock-vein matrix material showing equant grains of majorite-pyrope solid solution (MP) and irregular grains of magnesiowüstite (MW). (**B**) The SAED pattern of the magnesiowüstite ⟨111⟩ zone axis contains strong {220} reflections from the NaCl-type structure and weak superstructure-like reflections (arrows) from coherently intergrown inclusions. (**C**) The SAED pattern of the majorite-pyrope solid solution ⟨100⟩ zone axis indicates a cubic structure. The distinctive ⟨100⟩ patterns of tetragonal majorite were not observed.

and constitute 80% of the veins by volume; therefore, we maintain that they originated from the chondritic material by melting of silicates plus FeNi, FeS, and chromite during a shock-induced high-pressure and high-temperature event. Although experiments (*5*, *17*) show that magnesian silicate spinel [$Fe/(Mg+Fe) < 0.26$] transforms into perovskite plus magnesiowüstite at pressures greater than 23 GPa, the composition of the majorite-pyrope solid solution is inconsistent with such a disproportionation reaction. Because the olivine and low-Ca pyroxene in the unshocked region of the meteorite contain little Al, Na, and Cr, the majorite-pyrope solid solution could not have formed by direct transformation from these phases or their high-pressure equivalents, but rather crystallized from a melt that was enriched in Na_2O, CaO, and Cr_2O_3. The Na_2O, CaO, and Cr_2O_3 contents of the majorite-pyrope solid solution are quite similar to the concentrations of these elements in the bulk meteorite (Table 1), indicating that all of the Na, a majority of the Al and Ca, and part of the Cr in the melt were scavenged by the majorite-pyrope garnet. In addition, Cr_2O_3 was partitioned to magnesiowüstite, thus supporting the crystallization of this mineral pair from the Sixiangkou melt. Broad-beam EMPA analyses of the metal-troilite–poor matrix material revealed a composition identical to that of bulk Sixiangkou (Table 1). These findings lead to the conclusion that the shock event formed a silicate melt of Sixiangkou bulk composition (Table 1) and that both majorite-pyrope solid solution and magnesiowüstite crystallized from this melt under very high pressures and temperatures. The idiomorphic nature (8) and the high Na content of the majorite-pyrope solid solution argue against a solid-state transformation from a possibly preexisting Mg perovskite. The location of magnesiowüstite in the interstitial channels between garnet grains indicates that the garnet began to crystallize before magnesiowüstite and was therefore the liquidus phase in the Sixiangkou melt (Fig. 3). In addition to garnet and magnesiowüstite, the metal-poor matrix contains kamacite, troilite, magnetite, and a small amount of silicate glass along the magnesiowüstite and garnet grain boundaries (Fig. 3). On the basis of phase relations in the Mg_2SiO_4-Fe_2SiO_4 (*17*) and $MgSiO_3$ (*6*, *18*, *19*) systems and high-pressure melting experiments on peridotite (*20*) and the Allende carbonaceous chondrite (*21*), the majorite-pyrope garnet + magnesiowüstite assemblage crystallized from 2050° to 2300°C and 20 to 24 GPa. The presence of ringwoodite rather than wadsleyite in the polycrystalline lithology constrains the pressure to be greater than about 20 GPa, and the lack of perovskite or majorite-pyrope pseudomorphic cubes after perovskite in the fine-grained lithology indicates that the pressure during crystallization did not exceed about 24 GPa.

The large polycrystalline aggregate grains of ringwoodite and low-Ca majorite must have formed directly from olivine and low-Ca pyroxene through solid-state reactions without the incorporation of additional elements from the matrix melt. The composition and microstructures in the ringwoodite and majorite aggregate grains are indicative of polymorphic phase transitions from olivine and low-Ca pyroxene phenocrysts. Such microstructures have been produced experimentally (*16*, *19*), where large overstepping of equilibrium phase boundaries results in high nucleation rates and fine-grained polycrystalline aggregates. Similar polymorphic transformations of olivine and pyroxene to ringwoodite and majorite would be expected to occur at pressures between 20 and 24 GPa and temperatures in excess of 2000°C.

An anticipated short duration of the peak pressures and temperatures that prevailed during the passage of the shock wave (*10*) cannot account for (i) the solid-state transformation of olivine and low-Ca pyroxene to relatively coarse-grained aggregates of ringwoodite and majorite, respectively, (ii) the fusion of the low-pressure minerals and partial melting of the polycrystalline ringwoodite and low-Ca majorite, and (iii) the subsequent crystallization of majorite-pyrope garnet + magnesiowüstite from the dense silicate melt under high pressures and temperatures. The relatively coarse-grained nature of the polycrystalline ringwoodite and majorite (up to 6 and 10 μm, respectively) as well as organized walls of dislocations in majorite and the lack of disordered spinelloid structures in the ringwoodite argue for annealing at high pressure. These findings suggest that both lithologies were kept at high pressure and temperature for much longer than predicted by models of shock metamorphism (*10*). The apparent annealing of the microstructures could not have occurred after pressure release because the high-pressure phases of both assemblages did not transform back to their low-pressure polymorphs.

Shock experiments conducted on olivine or dunite have not produced any high-pressure polymorphs of olivine or pyroxene (*22*), and those conducted at 50 to 55 GPa and 467° to 727°C have only produced lamellae of diaplectic olivine glass (*23*). Although it may appear plausible that the peak pressure experienced by the shock veins in the Sixiangkou chondrite exceeded 24 GPa, the majorite-pyrope garnet + magnesiowüstite assemblage constrains the pressure-temperature conditions of crystallization. Our findings regarding crystallization

conditions and time scales in Sixiangkou shock veins cannot be explained by accepted shock models and therefore may warrant revision of such models. The relatively long time that the Sixiangkou shock veins remained in the pressure range of 20 to 24 GPa is inconsistent with transformations occurring during rapid decompression after the peak shock pressure was reached.

The conditions required for the formation of ringwoodite (γ) and wadsleyite (β) from olivine during shock events in ordinary chondrites are poorly constrained. Steele and Smith (*24*) and Stöffler *et al.* (*25*) suggest that special conditions, such as elevated temperatures of the target before shock compression, are required to transform olivine to ringwoodite. Such high temperatures were unlikely during the formation of Sixiangkou shock veins because they would have resulted in back transformation to the low-pressure phases after decompression. Scenarios suggesting peak pressures in excess of 50 GPa, as high as 80 GPa, were also developed (*26*). These models cannot be reconciled with our findings in Sixiangkou because there would be insufficient time available for the growth of relatively large ringwoodite and majorite grains with subgrain microstructures during the rapid decompression.

The composition and textural relations of the two high-pressure assemblages studied have important implications for (i) the pressure and temperature conditions that exist during dynamic events that lead to the formation of high-pressure polymorphs in chondritic meteorites, (ii) the duration of shock events in meteorites, and (iii) the crystallization of melts in shock veins. It may appear impossible to retain high pressures and temperatures for up to several seconds on the basis of shock experiments, but one can envisage that collisions of large asteroidal bodies or the passage of multiple shock waves through such bodies during complex collisional events could account for such conditions.

REFERENCES AND NOTES

1. A. E. Ringwood and A. Major, *Phys. Earth Planet. Inter.* **3**, 89 (1970); *Earth Planet. Sci. Lett.* **12**, 411 (1971); C. R. Bina and B. J. Wood, *J. Geophys. Res.* **92**, 4853 (1987); T. Katsura and E. Ito, *ibid.* **94**, 15663 (1989); M. Akaogi, E. Ito, A. Navrotsky, *ibid.*, p. 15671.
2. A. J. Brearley, D. C. Rubie, E. Ito, *Phys. Chem. Miner.* **18**, 343 (1992).
3. A. J. Brearley and D. C. Rubie, *Phys. Earth Planet. Inter.* **86**, 45 (1994).
4. T. G. Sharp, G. Y. A. Bussod, T. Katsura, *ibid.*, p. 69.
5. E. Ito, E. Takahaschi, Y. Matsui, *Earth Planet. Sci. Lett.* **67**, 238 (1984).
6. T. Kato and M. Kumazawa, *Nature* **316**, 803 (1985).
7. A. Putnis and G. D. Price, *ibid.* **280**, 217 (1979); G. D. Price, A. Putnis, D. G. W. Smith, *ibid.* **296**, 727 (1982); G. D. Price, *Phys. Earth Planet. Inter.* **33**, 137 (1983); M. Madon and J. P. Poirer, *ibid.*, p. 31.
8. M. Chen and A. El Goresy, *Meteoritics* **29**, 456 (1994); M. Chen, T. G. Sharp, B. Wopenka, A. El Goresy, X. Xie, in preparation.
9. H. Mori and H. Takeda, *Lunar Planet. Sci.* **XVI**, 579 (1985).
10. T. H. Ahrens and J. Rosenberg, in *Shock Metamorphism of Natural Materials: Proceedings of the First Conference*, B. M. French and N. M. Short, Eds. (Mono Book, Baltimore, MD, 1968), p. 59; B. French, *ibid.*, p. 1; J. Reinhart, *ibid.*, p. 31; P. S. De Carli, *ibid.*, p. 129; E. C. T. Chao, *ibid.*, p. 135; M. R. Dence, *ibid.*, p. 169; P. B. Robertson, *ibid.*, p. 169; E. C. T. Chao, J. B. Best, J. A. Minkin, *Proc. Lunar Planet. Sci. Conf.* **3**, 907 (1972).
11. F. Guyot, G. D. Gwanmesia, R. C. Liebermann, *Geophys. Res. Lett.* **18**, 89 (1991).
12. N. Doukhan, V. Sautter, J. C. Doukhan, *Phys. Earth Planet. Inter.* **82**, 195 (1994).
13. S. Heinemann, unpublished material.
14. S.-I. Karato, D. C. Rubie, H. Yan, *J. Geophys. Res.* **98**, 9761 (1993).
15. R. Angel *et al.*, *Am. Mineral.* **74**, 509 (1989).
16. Y. Wang, T. Gasparik, R. C. Liebermann, *ibid.* **78**, 1165 (1993).
17. E. Ito and E. Takahashi, *J. Geophys. Res.* **94**, 10637 (1989).
18. S. K. Saxena, N. Chatterjee, Y. Fei, G. Shen, *Thermodynamic Data on Oxides and Silicates* (Springer, Berlin, 1993).
19. A. Hogrefe, D. C. Rubie, T. G. Sharp, F. Seifert, *Nature* **372**, 351 (1994).
20. J. Zhang and C. Herzberg, *J. Geophys. Res.* **99**, 17729 (1994).
21. C. B. Agee, *Nature* **346**, 834 (1990).
22. G. D. Price, A. Putnis, O. Agrell, *Contrib. Mineral. Petrol.* **71**, 211 (1979).
23. R. Jeanloz, *Science* **197**, 458 (1977).
24. I. M. Steele and J. V. Smith, *Lunar Planet. Sci.* **IX**, 1101 (1978).
25. D. Stöffler, K. Keil, E. R. D. Scott, *Geochim. Cosmochim. Acta* **55**, 3845 (1991).
26. C. M. Lingemann and D. Stöffler, *Meteoritics* **29**, 491 (1994).
27. H. Wang, Y. Li, F. Zhang, C. Lin, *Lunar Planet. Sci.* **XXVI**, 1463 (1995).
28. The bulk composition of the chondrite in percent by weight, as determined by Wang *et al.* (*27*): 38.94 SiO_2, 24.54 MgO, 1.88 CaO, 0.35 MnO, 15.84 FeO, 0.10 TiO_2, 2.62 Al_2O_3, 0.55 Cr_2O_3, 1.01 Na_2O, 0.11 K_2O, 0.20 P_2O_5, 6.02 Fe, 1.21 Ni, and 6.00 FeS; total, 99.37 weight %.

29. B.W. was supported by NSF grant GER 9023520.

18 August 1995; accepted 27 November 1995

Iridium Metal in Chicxulub Impact Melt: Forensic Chemistry on the K-T Smoking Gun

Benjamin C. Schuraytz,*† David J. Lindstrom, Luis E. Marín, René R. Martinez, David W. Mittlefehldt, Virgil L. Sharpton, Susan J. Wentworth

Iridium concentrations in successively smaller subsplits of melt rock and melt breccia from the Chicxulub impact basin were tracked to isolate and identify iridium carrier phases. Iridium-rich particles were isolated from two samples, and a micrometer-scale, silicate-enclosed aggregate of subhedral iridium metal grains was identified in one, confirming earlier reports of iridium at ground zero of the impact at the Cretaceous-Tertiary (K-T) boundary. The aggregate may be either a phase formed after the collision or a relict of the Chicxulub basin-forming meteorite. In either case, its presence indicates that even among the largest impact structures on Earth, meteoritic components may be preserved within the crater.

Of all the elements in the periodic table, iridium (Ir) figures most prominently as a chemical fingerprint of meteorite impact events in shock-metamorphosed target rocks and ejecta on the Earth and moon (*1*). Discovery of anomalously high concentrations of Ir coincident with the K-T boundary, the worldwide stratigraphic horizon defined by a major biological mass extinction event 65 million years ago, led to the hypothesis that impact of an Earth-crossing asteroid ~10 km in diameter was responsible for the sudden influx of Ir and the ensuing biological crisis (*2*). All available evidence points to the Chicxulub structure—buried beneath Mexico's Yucatán peninsula, with diameter estimates of 180 to 300 km—as the site of the K-T impact (*3–6*).

Definitive constraints on the nature of the impacting body (whether asteroid or comet), in terms of size, velocity, and possible compositional correlation with other meteorites (*7*), are yet to be determined. Anomalously high Ir concentrations in some Chicxulub samples (*4, 8*) suggest that melt rocks within the crater may provide additional constraints on the nature and fate of the projectile. To better understand the partitioning of projectile material between crater deposits and ejecta, we began a search for physically identifiable carrier phases of Ir and other siderophile elements within these melt rock samples (*9, 10*). We discovered an Ir metal particle enclosed in

B. C. Schuraytz and V. L. Sharpton, Lunar and Planetary Institute, Houston, TX 77058, USA.
D. J. Lindstrom, Planetary Science Branch, SN4, NASA Johnson Space Center, Houston, TX 77058, USA.
L. E. Marín, Instituto de Geofísica, Universidad Nacional Autónoma de México, Coyoacan 04510, México D.F.
R. R. Martinez, D. W. Mittlefehldt, S. J. Wentworth, Lockheed Martin, Engineering and Sciences, Houston, TX 77058, USA.

*To whom correspondence should be addressed.
†Present address: Planetary Science Branch, SN4, NASA Johnson Space Center, Houston, TX 77058, USA.